Physics – Uspekhi **67** (4) 390 – 404 (2024) ©2024 Uspekhi Fizicheskikh Nauk, Russian Academy of Sciences

CONFERENCES AND SYMPOSIA PACS number: 95.55.Vj

Modern silicon detectors for gamma-ray astrophysics

E M Verbitskaya, V K Eremin

DOI: https://doi.org/10.3367/UFNe.2023.04.039531

Contents

Abstract. A steady trend in improving gamma-ray telescopes is the creation of their 3D sensitive medium, trackers based on silicon position-sensitive detectors. Among them, planar double-sided silicon strip detectors (DSSDs) are planned to be used in space telescopes of international observatories and the Russian HERMES project. The characteristics of DSSDs prototype for the e-ASTROGAM and HERMES telescopes are presented, and critical elements of the detectors are discussed. The reality of creating silicon trackers based on the physical background and technologies for the development of silicon detectors in Russia is shown.

Keywords: gamma-ray space telescopes, trackers, silicon planar detectors, double-sided strip detectors, voltage terminating structures

1. Introduction

The modern development of experimental astrophysics generally repeats the recent history of work in high energy physics (HEP), where building the giant detecting systems has become a key element. They combined both various types of detectors and large numbers of them, which led to a qualitative change in technology, of which silicon detectors are the most striking example. The topology of these devices has fundamentally changed, with the reproducibility of characteristics in large batches, the reliability, and the radiation hardness improved. This trend is also important for astrophysics, where, e.g., in planned space gamma-ray telescopes, the area of silicon detectors will be comparable to that used in inner trackers of Large Hadron Collider (LHC) experiments at CERN, Switzerland. In this connection, it is reasonable to begin a consideration of the role of silicon detectors in gamma-ray astrophysics from an excursus into the physics and technology of semiconductor detectors for HEP.

Indeed, semiconductor detectors as a class of devices for wide-range applications appeared in relation to the problems of HEP and nuclear physics [1–4] with creating accelerating facilities of a new generation, such as LHC, the Relativistic Heavy Ion Collider (RHIC) in the Brookhaven National Laboratory, USA, and the Facility for Antiprotons and Ions Research (FAIR) at the GSI Helmholtz Centre for Heavy Ion Research, Germany. To build experimental facilities at these accelerators, it was necessary to develop a measurement base with a new level of characteristics to monitor the processes of interaction of particles, such as protons, with energies up to several TeV.

The problem was solved by moving to devices consisting of many position-sensitive detectors that form a three-dimensional space capable of recording all the events occurring in it and linking them to a time scale. The most complex problem was to implement this approach at the LHC in the region maximally close to the intersection point of colliding proton beams, where the necessary accuracy of trajectory fixation is a few microns. The solution was to create so-called inner trackers using silicon detectors of relativistic particles [2], which stimulated the development of the physics and technology of silicon detectors, making them widely used devices.

It is also worth noting that detector requirements related to identifying their characteristics in large batches, long-term stability, and radiation hardness have changed, leading to a revision in understanding detector operation. The question arose of quantitatively predicting the scenario of degradation of characteristics up to doses at which it is impossible to continue the experiment without changing detectors. To solve this problem, at CERN, international research and development (RD) collaborations have been organized to study the radiation effects on silicon and their manifestation in the characteristics of detectors important for LHC experiments, to develop detector degradation scenarios, and to design new types of detectors. In connection with the LHC upgrade, consisting of a stepwise ten-fold increase in the relativistic proton beam luminosity up to 10^{34} cm^{-2} s^{-1} and the proton

E M Verbitskaya (*), **V K Eremin** (**)
Ioffe Institute, Russian Academy of Sciences,
ul. Politekhnicheskaya 26, 194021 St. Petersburg, Russian Federation
E-mail: (*) elena.verbitskaya@mail.ioffe.ru,
(**) Vladimir.Eremin@mail.ioffe.ru

Received 21 April 2023
Uspekhi Fizicheskikh Nauk **194** (4) 416 – 431 (2024)
Translated by V L Derbov

energy to 14 TeV (High Luminosity Large Hadron Collider, HL-LHC) [5], new designs of segmented 2D and 3D silicon detectors were developed, which allowed a substantial improvement in their position resolution, operation speed, and radiation hardness [2, 6–9]. Great attention was paid to the reproducibility of detector characteristics by testing detectors at the stage of mass production in amounts measured in tens and hundreds of square meters.

Similar problems arise in astrophysics. A traditional instrument in studies of cosmic gamma radiation is gamma-ray telescopes using scintillation detectors, the best known of which is the Imaging Compton Telescope (COMPTEL), one of the four telescopes of the Compton Gamma Ray Observatory (CGRO) [10]. At the same time, at the Gamma-Ray Large Area Space Telescope (GLAST) space observatory, at present called the Fermi Gamma-Ray Space Telescope (FGST or FGRST), functioning in space since 2008, one of the two systems is the Large Area Telescope (LAT), containing a silicon tracker [11].

An urgent problem in this field is increasing the angular and energy resolution of telescopes. Thus, during the last 20 years, proposals have appeared on creating MEGA and e-ASTRO-GAM space observatories [12, 13], in the telescopes of which, along with scintillators, it is planned to install position-sensitive silicon detectors. A similar project is proposed by Russia and is called the High-Performance MeV Spectrometer (HERMES) [14]. In this connection, the analysis of critical questions determining the successful realization of plans becomes an important issue, a survey of which is given in this paper. It is motivated by a presentation on state-of-the-art of silicon planar detectors made at a scientific session of the Department of Physical Sciences of the Russian Academy of Sciences, "Gamma quanta and neutrinos from space: what we see now and what is needed to see more," held at the Ioffe Institute on April 22, 2023.

Below, we describe the principle of the functioning of silicon detectors of nuclear radiation and the latest desingns of silicon detectors aimed at using planar technology for their mass production, approved in HEP and promising for space gamma-ray telescopes. A description of space observatories is given, in which silicon detectors already function or are planned for use. The Ioffe Institute plans to create a gamma-ray telescope, and its experience in researching and developing silicon detectors as a base for their implementation is presented.

2. Silicon planar detectors of nuclear radiation

The parent structure of silicon radiation detectors [1–4] the one based on electron-hole junction, p^+-n-n^+ or n^+-p-p^+ types, in which the n- or p-type silicon (Si) has a high resistivity (up to a few ten kΩ cm) that forms the sensitive volume of the detector, and the p- and n-layers are strongly doped contacts. When reverse, i.e., depleting, voltage V is applied to the detector, a sensitive region is formed — the region of the electric field (i.e., the space charge region (SCR)) — in which the charge generated by the radiation acting on the detector is collected. The thickness of the contacts is about a few micrometers, which is substantially smaller than that of the sensitive volume, which usually does not exceed 1 mm.

The most important characteristic of a detector based on an electron-hole junction is the electric field distribution $E(x)$, where x is the coordinate normal to the surface. It can be found from the Poisson equation [15]:

$$-\frac{\mathrm{d}^2\varphi(x)}{\mathrm{d}x^2}=\frac{\mathrm{d}E(x)}{\mathrm{d}x}=\frac{\rho(x)}{\varepsilon_0\varepsilon_{\mathrm{Si}}}\,, \tag{1}$$

where φ is the potential arising upon application of voltage V, ε_0 is the dielectric constant, and $\varepsilon_{\mathrm{Si}}$ is the silicon permittivity. The solution to Eqn (1) with the charge density ρ, where $\rho(x)=eN_0$ (N_0 is the concentration of dopant impurity in the high-resistivity silicon), yields a linear distribution of $E(x)$ in the SCR with thickness w over the coordinate x:

$$E(x)=-\frac{eN_{\mathrm{eff}}}{\varepsilon_0\varepsilon_{\mathrm{Si}}}\,(x-w)\,, \tag{2}$$

where N_{eff} is the effective concentration of space charge (in an unexposed detector $N_{\mathrm{eff}}=N_0$), and w is determined by the value of V:

$$w=\sqrt{\frac{2\varepsilon_0\varepsilon_{\mathrm{Si}}V}{eN_{\mathrm{eff}}}}\,. \tag{3}$$

The effect of irradiation by hadrons (protons, neutrons), electrons, etc. leads to particle energy transfer to the atoms of the silicon crystal lattice. This energy is mainly spent for generating nonequilibrium charge carriers and forming primary defects (vacancy–interstitial pairs) in the lattice. In the case of irradiation by neutrons, the defect formation is a dominating process [1, 2, 6]. Primary defects form complexes of vacancies and interstitials with dopant and residual impurities in silicon, the vacancies coupling to each other to form divacancies or clusters of defects. The formation of radiation-induced defects impairs steady-state volt-ampere (I-V) characteristics of the detectors. As the irradiation dose increases, the dark current monotonically grows, which leads to an increase in the current component of the device noise.

Radiation-induced nonequilibrium carriers drift in the SCR of the detector, generating a signal — the electric response to the detected particle, i.e., current i or charge Q, induced at the structure electrodes (depending on the input resistance of the recording electronics). According to the Shockley–Ramo theorem, the current signal i caused by a point charge q_0 is expressed as [16]

$$i(t)=q_0E_{\mathrm{w}}v_{\mathrm{dr}}\big(x(t),T\big)\,, \tag{4}$$

where v_{dr} is the drift velocity of charge q_0 (electrons or holes), depending on E, time t, and temperature T [17]. The parameter E_{w} is the so-called weighting field measured in [cm^{-1}], for a nonsegmented detector equal to $1/d$, where d is the detector thickness. Thus, for structures in which the p^+-n junction linear dimensions are much larger than d, the induced current is related to the drift velocity of a compact cloud of nonequilibrium carriers as

$$i(t)=\frac{q_0}{d}\,v_{\mathrm{dr}}\big(x(t)\big)\,. \tag{5}$$

The drift time of the carriers is determined by the value of v_{dr}, i.e., the electric field, and, at the saturated velocity and the standard detector thickness of hundreds of mm, it amounts to units of nanoseconds [17]. In the case of a particle track comparable to the thickness of the sensitive region, and even more so when detecting high-energy particles whose range

exceeds d, the kinetics of the current $i(t, T)$ is calculated by summing the layer-wise contributions of the drift of generated charges, which usually requires numerical methods. However, the simple Eqn (5) is widely used to study detectors in the transient current technique (TCT). For a uniform distribution of the field, the current signal kinetics is determined by the trapping time constant of drifting carriers τ and described by the exponential expression

$$i(t, T) = \frac{q_0}{d}\mu(T)E\exp\left(\frac{t}{\tau}\right). \quad (6)$$

In unexposed detectors, τ is a few ms (as in the initial silicon).

The development of detectors for LHC experiments affected the optimization of properties of high-resistivity silicon and complexification of instrumentation design and manufacture technology [1, 2, 6, 9]. The simplest structure of a silicon detector is a detector with one nonsegmented p–n junction (the so-called pad detector), manufactured by means of planar technology methods of microelectronics as a base for creating a more advanced type of detector.

We should explain the term 'planar' used for these detectors, which implies that all elements of the detector are located on one or two planar sides of a wafer. The layers created on the planar surface of a silicon wafer are structured by the photolithography method, which provides the necessary characteristics of the detector. Usually, the surface structure of the detector includes three layers: contact n^+ and p^+ conducting layers doped with atoms of donor or acceptor impurity, respectively, a layer of isolating silicon dioxide SiO_2, and a layer of metal (aluminum) to connect the doped layers with the instrumentation recording electric signals. The topology and characteristics of the layers implement the required detector sensitivity to the detected radiation and stable I-V characteristics of the detector without using mechanical volumetric structuring of the wafer (e.g., making bevels, creating grooves, or applying protective pastes). This absence allows precise control and reproducibility of technological operations, i.e., the automation of the technological process, which is the main advantage of planar technology.

Note that planar technology is the base of most microelectronic devices, due to which the equipment used and the processing of silicon wafers are a result of in-depth research and are optimized for the aims of the huge market of produced devices. Silicon detectors qualitatively differ from microelectronic devices in their purpose, and their difference is illustrated in Table 1, where typical dimensional and electric characteristics of both types of devices are presented.

The comparison shows a complete discrepancy between the characteristics and requirements, even though the set of technological operations is the same. The technologies differ only in particular regimes of carrying out the operations. This is exactly why it is possible to obtain detectors with an area of up to 100 cm^2 on the original wafer with a diameter of 150 mm with acceptable yield, avoiding even a single defect able to violate the required properties of the device. In the production of digital chips, such a defect can disable only one device, which is unessential for their number on a wafer measured by hundreds.

Figure 1 shows a part of the surface of a nonsegmented p^+-n-n^+ detector based on n-Si, on the upper side of which a p^+-n junction is formed, and the highly doped n^+-region is the back ohmic contact. The initial wafer from tens to hundreds of microns thick forms a sensitive n-type volume. As a rule, at the detector periphery, a system of isolated guard ('floating') p^+-rings (a voltage terminating structure, VTS) is created, in which the intersegment isolation is implemented using SiO_2. This structure provides a smooth decrease in the potential at the detector periphery, preventing a breakdown (see Section 4 for details). Nonsegmented detectors allow the spectrometry of quanta and particles with high energy resolution, but they possess no position sensitivity and are mainly intended for experiments in nuclear physics and monitoring the operation of energy plants.

Table 1. Characteristics of silicon-based detectors and digital chips.

Characteristic	Detector	Digital chip
Area, mm^2	up to 10^4	1 – 10
Active region volume, mm^3	up to 10^5	$< 10^{-2}$
Operating voltage, V	10 – 1000	1 – 5
Charge transfer length, mm	up to 10	10^{-3}
Main technological operations	Oxidation, ion implantation, photolithography	
Critical requirements	High purity of volume, high operating voltage	Small size of elements, low power consumed

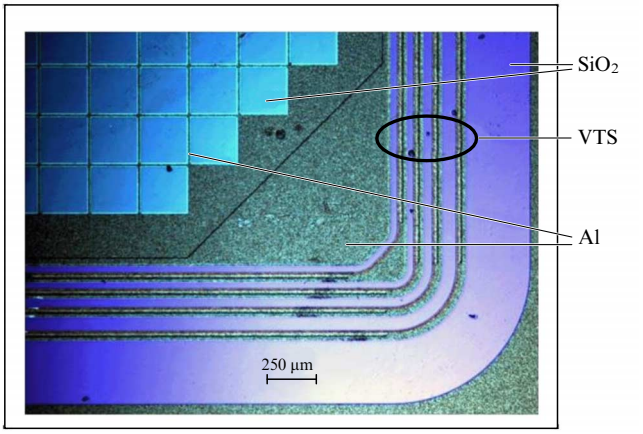

Figure 1. Photograph of part of a silicon detector surface with a system of VTS guard rings.

At present, the main raw material for detectors used at the LHC is high-resistance p-type silicon with a resistivity of no less than 5 kΩ cm and, naturally, it is the n^+–p junction that plays the main role. This is due to the optimization of the detector structure for operating under high radiation loads, since, in the exposed n^+-p-p^+ structure, the maximum of the electric field is stably located near the n^+-contact independent of the irradiation dose. This minimizes the time of nonequilibrium carrier collection, which increases the signal in a heavily irradiated detector compared to the p^+-n-n^+ structure.

To realize the position resolution, planar detectors have been developed, in which the p^+-n- or n^+-p junction was segmented; foremost among them are strip and pixel structures, briefly described below.

Single-sided strip detectors (SSSDs or SSDs) with segmented contacts on the side with the junction (p^+-n or

n^+-p) are the most in demand both in the HEP and in nuclear physics. The strips are p^+-n or n^+-p strip-shaped junctions with a pitch (step) from tens to hundreds of microns [1, 2, 18–20], each connected to the recording electronics, which allows getting information from an individual strip. To prevent the electric connection of n^+ strips in the n^+-p-p^+ structure, separating regions of p-silicon are created between them (the so-called p-spray or p-stop), where the boron concentration is 2–3 orders of magnitude lower than in a p^+-contact [2, 21]. The SSSDs provide single-coordinate sensitivity with a resolution of units of microns and are characterized by high energy and time resolution. So, in experiments with heavy ions at GSI, a time resolution of 14 ps has been reached [22, 23].

Pixel detectors were developed for reaching high-precision 2D position sensitivity in intense fields of detected particles. In such a design, the n^+-p-p^+ junction in the n^+-p structure is segmented in an array of isolated junctions [19, 24]. The pixel size can vary from hundreds of square microns to a few square centimeters. In such detectors, it is also necessary to create separating p^+ layers on the n^+ side. Such a topology not only allows obtaining the required 2D position resolution but also provides a high speed of particle detection in the regime of independent signal readout from each individual pixel. In this case, the number of electronic channels is determined by the product $A_x \times A_y$, where A_x and A_y are the numbers of channels along the x and y axes, respectively, and the connection with electronics is usually provided by contacting the bumps of the detector chip pixels with the electronic chip (so-called bump bonding).

Double-sided p^+-n-n^+ and n^+-p-p^+ strip detectors (DSSDs) with orthogonal strips on both sides of the detector [2] have found less application than SSSDs have because of the more complex technology [25, 26]. The main advantage of these detectors is two-dimensional position sensitivity; the number of electronic channels is $A_x + A_y$, and the signal readout is implemented using multi-channel conditioning amplifiers.

Low-gain avalanche detectors (LGADs) having the $n^{++}-p^+-p-p^{++}$ structure based on high-resistivity p-Si (Fig. 2) have been developed to keep the signal magnitude sufficient at operating voltages of 500 V and the radiation doses F at more than 1×10^{15} equivalent neutrons/cm^2 (the neutron energy being 1 MeV) [2, 8, 27, 28]. The signal amplification in an LGAD occurs at the expense of the avalanche multiplication of charge carriers in a thin (~ 2 μm) built-in p^+ layer doped with boron, where the electric field reaches a magnitude sufficient for impact ionization, and the signal gain coefficient amounts to a few ten. Measurements of the characteristics of the exposed detectors have shown a decrease in the gain [29], which was partially suppressed by doping the built-in p^+ layer with gallium [30]. To improve the timing characteristics, thin (~ 50 μm) LGADs with an optimized structure and active area of a few mm^2 were developed, in which an operation speed of 30 ps was implemented [28, 31].

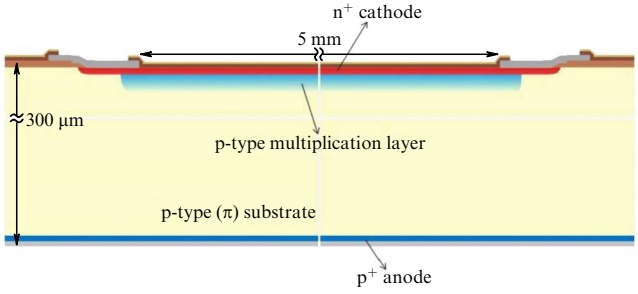

Figure 2. Schematic section view of LGAD detector [27].

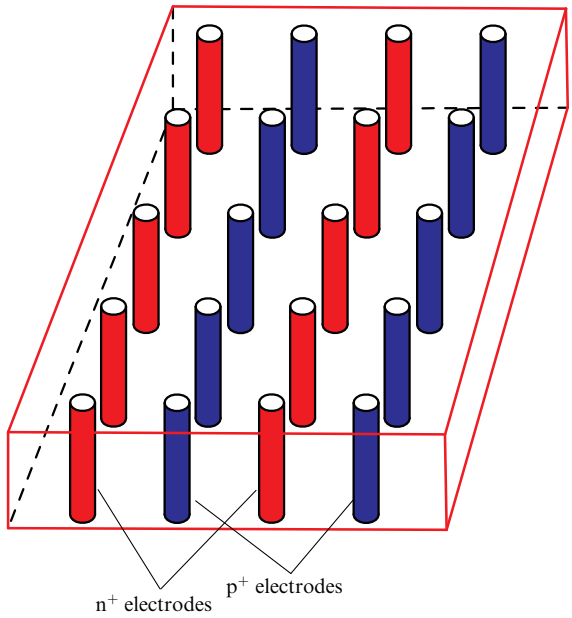

Figure 3. Schematic image of 3D detector structure [2].

3D detectors are those with 3D profiling of the sensitive volume, in which the junctions are shaped by creating single or alternating p^+ and n^+ 'wells' perpendicular to the surfaces of the silicon wafer and arranged as an array with a distance of tens of microns between them (Fig. 3). It should be noted that detectors of this type possess no 3D sensitivity, and the term 3D in their name indicates only the deep profiling of their sensitive volume. This type of detector was also developed to decrease the operational voltage, to improve the operation speed, and to broaden the range of radiation hardness [32–36]. The thickness of the region between the n^+ and p^+ 'wells', i.e., carrier collection length on which the signal is formed, is substantially smaller than in usual SSSDs, which decreases the dose dependence of the signal. A serious drawback of 3D detectors is the complexity of their manufacturing process, completed by the operations of deep plasma etching of the 'wells' and filling them with doped polycrystalline silicon. Therefore, the sensitive area of individual detectors does not exceed a few square centimeters.

It is worth noting that the above detectors, including nonsegmented ones, are complex devices requiring much more advanced technologies, which have nevertheless already been developed, and the detectors are used on a scale satisfying the needs of HEP.

In the LHC upgrade to reach the beam parameters relevant to the HL-LHC, the maximum dose of radiation acting on silicon detectors placed as close as possible to the point of proton beam intersection will reach 2×10^{16} equivalent neutrons/cm^2, i.e., will increase by nearly 10 times [2, 5] compared to the LHC, which will inevitably lead to the degradation of their characteristics. The main criterion of detector operability in such situations is

the signal-to-noise ratio, which should be no less than 10 when detecting relativistic hadrons, whose energy deposition in silicon amounts to nearly 100 keV. For silicon planar detectors with a sensitive region thickness of 300 μm, this can be implemented up to the dose $F \sim 10^{15}$ equivalent neutrons/cm^2 by optimizing the characteristics of the silicon and detector design.

Degradation of the main characteristics of silicon detectors is associated with the introduction of radiation defects, which are centers of current generation and nonequilibrium carrier trapping [37]. The dependence of the characteristics on the radiation dose is determined by the following relations:

• the growth of dark generation current I [2, 38]:

$$\frac{I}{V_w} = \alpha F_{\rm eq}\,, \tag{7}$$

where $\alpha = 4 \times 10^{-17}$ A cm^{-1} is the current degradation rate under irradiation, V_w is the volume of the region where the current generation occurs;

• the growth of effective concentration $N_{\rm eff}$ [2, 38]:

$$N_{\rm eff} \approx g F_{\rm eq}\,, \tag{8}$$

where g is the $N_{\rm eff}$ rate constant, equal to 0.004–0.04 cm^{-1}, depending on the grade of silicon;

• the time constant of charge carrier trapping by the defect energy levels [39]:

$$\tau^{-1} = \beta F_{\rm eq}\,, \tag{9}$$

where the proportionality coefficient β depends on the type of radiation, as well as on the grade of silicon from which the detector is made. For hadrons, β amounts to $(4-7) \times 10^{-16}$ cm^2 ns^{-1}, whereas, for ions, this value is substantially greater and depends on their mass and charge.

The results of multiple studies aimed at establishing the effect of irradiation on the characteristics of silicon detectors used in HL-LHC experiments and developing their radiation degradation scenario are presented in Ref. [2], Chapter 21 (see also references therein), where the issues considered in Section 2 are described in detail.

3. Silicon detectors as an element of instrument base of space gamma-ray observatories

Gamma quanta are one of the components of electromagnetic cosmic radiation, the energy spectrum of which encompasses a huge range (more than 30 orders of magnitude) from radio waves to quanta with superhigh energies of the order of 10^{20} eV (Fig. 4) [40]. Currently, gamma-ray astrophysics is a relevant and actively developing field of astronomy, since it offers a possibility to study fundamental physical processes that accompany fast conversion and release of energy in many space objects. In contrast to charged particles, gamma quanta are not deflected by electric and magnetic fields and possess higher penetration ability. That is why their detection can be used to determine the position of the radiation source. According to modern concepts, cosmic gamma radiation is divided into two classes: diffuse radiation, more or less uniformly filling our Galaxy, and discrete radiation, so-called gamma bursts, generated in local cosmic objects, the nature of which is not entirely clear.

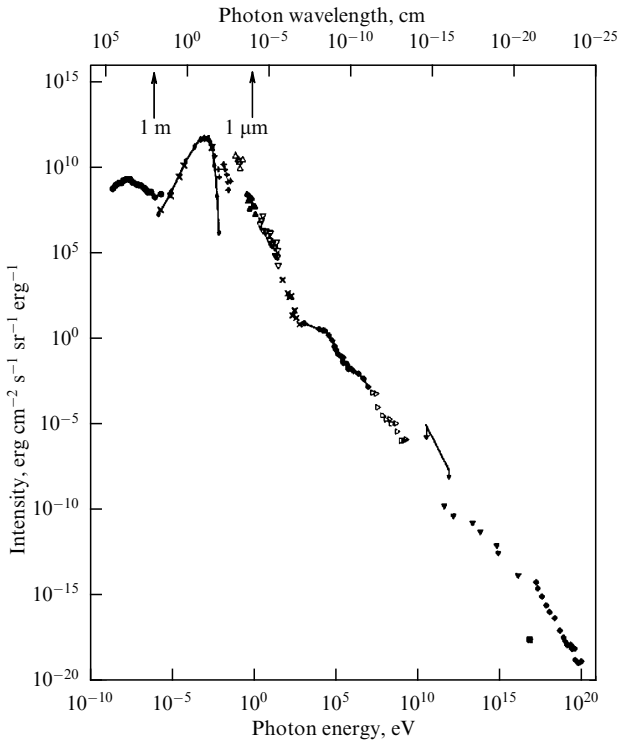

Figure 4. Joined photon spectrum of diffuse extragalactic background radiation. Plot is a compilation of a large amount of experimental data [40].

Below, we list the main processes that occur when a gamma quantum passes through matter [3]:

• photoelectric effect — a transfer of the entire energy of the gamma quantum to one of the atomic electrons, which then spends it according to the mechanisms of interaction of electrons with a solid, thus making possible gamma-ray spectrometry;

• Compton effect — the scattering of a gamma quantum by an electron. In this case the electron acquires only a part of the gamma quantum energy, and the process of absorbing the entire quantum energy is multistage. As a result of each event of gamma quantum–electron interaction, the energy of the quantum and the direction of its propagation change, which allows reconstructing the quantum propagation direction before the first scattering event in the detecting medium;

• pair creation effect — the gamma quantum in the electric field of a nucleus produces an electron–positron pair ($e-e^+$). The process has a threshold gamma quantum energy $E_\gamma = 1024$ keV and dominates at E_γ higher than ~ 10 MeV; in this case, the pair creation cross section grows with an increase in E_γ and depends on the nuclear charge Z as Z^2;

• nuclear photoelectric effect — at energies above several ten MeV, a gamma quantum is capable of knocking nucleons out of the nucleus, creating isotopes or nuclei of other elements.

Ground-based gamma-ray observatories make a significant contribution to the study of the Universe. With the growth of energy, the intensity of the gamma quantum flux rapidly falls (Fig. 4); therefore, for its efficient detection, it is necessary to use detectors with the total area exceeding hundreds of square meters, which is practically impossible for orbital systems. A traditional tool for ground-based research is Cherenkov telescopes, whose cameras record

bursts of Cherenkov radiation from relativistic particles that make up extensive atmospheric showers initiated by primary gamma rays and reaching Earth from deep space objects. The cameras of most modern Cherenkov telescopes, e.g., the Very Energetic Radiation Imaging Telescope Array System (VERITAS) [41], incorporate vacuum photomultipliers that suffer from several drawbacks, such as relatively low detection efficiency (not greater than 30%), high operating voltage, considerable dimensions, and the possibility of complete failure under excess exposure. An alternative option is silicon photomultipliers (SiPMs), which have recently been brought to mass production and are included in the designs of cameras of new generation Cherenkov gamma-ray telescopes currently being developed [42, 43].

Space-based gamma-ray astronomy is an independent field that completes terrestrial research in the range of low-energy quanta. Placing telescopes in space makes it possible to detect electromagnetic radiation to which Earth's atmosphere is not transparent. The Compton Telescope COMPTEL [10], launched on the Space Shuttle Atlantis on April 5, 1991 and operated until June 4, 2000, was one of the four Compton Gamma-ray Observatory (CGRO) telescopes with the largest payload at that time (17 t). The telescope was intended to determine the position of the sources of gamma quanta in the range of 0.75–30 MeV and had a large field of view of about 1 sr. It included two detector arrays: an upper one based on an NE 213 A liquid scintillator, and a lower one using a scintillator based on NaI(Tl). The gamma quanta were detected due to Compton scattering in the upper detector and their subsequent recording in the lower detector. The achieved telescope characteristics — an angular resolution when determining the position of the gamma radiation source of the order of 1° and energy resolution of 5–10% FWHM — are still the standard when comparing the expected characteristics of programs of gamma-ray observatories proposed in the last decade (see below). It was noted that the accompanying spectral lines in the range of 1–3 MeV, found in the Orion constellation, were the threshold of sensitivity for the COMPTEL telescope [44]. Based on the studies carried out with the telescope, a catalogue of gamma radiation sources was composed, including 32 permanent sources and 31 source of gamma-ray bursts [45].

During the last 15 years, silicon segmented planar detectors have been actively introduced into the instrumental base of gamma-ray astrophysics. Silicon proves itself to be the best material for creating devices aimed at recording the trajectories of gamma quanta, taking into account its relatively low atomic number, which determines the domination of the Compton effect at least within the energy range of units of MeV, as well as the last technological achievements in creating strip detectors and electronics for signal recording and processing. Development of these detectors, including those for gamma-ray telescopes planned for the future, is largely based on the experimental studies carried out within the programs and experiments in HEP and nuclear physics. The main requirements for gamma radiation detectors are largely like those for detectors for HEP and nuclear physics: high position and energy resolution in the detection of secondary particles — electrons and $e-e^+$ pairs formed in the interaction of gamma quanta with the detecting medium, and an operating speed that allows performing the analysis of the recorded events. Below, we provide a brief description of some gamma-ray observatories that are employing or planning to use silicon segmented detectors.

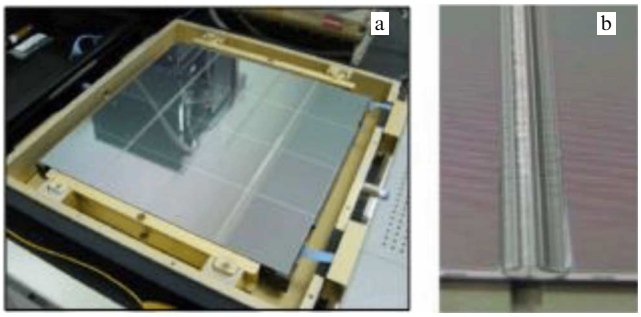

Figure 5. (a) Assemblage of 16 microstrip detectors in one layer of the Fermi-LAT telescope; (b) part of the layer of the LAT tracker with interstrip connections of two SSSDs by the ultrasound welding method (wire bonding) [11].

In the Gamma-ray Large Area Space Telescope (GLAST) observatory, currently the Fermi Gamma-ray Space Telescope (FGST or FGRST) intended to study radiation in the range of energies from 20 MeV to 300 GeV, one of the two systems is the Large Area Telescope (LAT) [11], including a tracker for converting the incident gamma radiation into $e-e^+$ pairs in the corresponding energy range and tracing the trajectories of the pairs in order to determine the position of the gamma radiation source. In the LAT tracker, SSSDs (the authors use the abbreviation SSD — single-sided detector) and standard electronics for signal recording are used [11, 46].

At the beginning of the 21st century, the LAT tracker was the largest detecting system based on SSSDs, providing low energy consumption and noise levels. At the development stage, 11,500 detectors were manufactured by the Hamamatsu Photonics Co. based on n-Si wafers with a diameter of 150 mm and thickness of 400 μm; they had p^+ strips, each integrating a separating capacitor. An individual SSSD had an area of 8.95×8.95 cm^2 and included 384 strips with a pitch of 228 μm. The total and sensitive areas of the tracker amounted to ~ 74 m^2 and 2 m^2, respectively. Each module of the tracker had 18 planes, consisting of two layers (x and y) of SSSDs, which provided 2D sensitivity. The 16 planes in the upper part of the tracker alternated with the convertor material with high Z (tungsten). An array consisting of 16 SSSDs in one layer of the LAT module is presented in Fig. 5.

When launching the LAT in 2008, the tracker included 16 modules, a segmented anticoincidence system that shielded the tracker from background events, and a programmable trigger and data acquisition system [46]. Each module was a vertical set of 18 planes, including x and y SSSDs and tungsten layers. The SSSDs detected the passage of charged particles by measuring the tracks of the arising $e-e^+$ pairs, which was used to reconstruct the location of the source of the incident gamma quanta. The tracker included 880 thousand signal-reading channels. The structure of the LAT was optimized by Monte Carlo simulation. The preliminary verification of the structure and the results from simulations of the characteristics was carried out in a series of tests on the beams in the Stanford Linear Accelerator Center (SLAC), CERN, and GSI.

The results obtained confirmed that the LAT tracker meets, and often even exceeds, the design and performance requirements. In 2019, the National Aeronautics and Space Administration (NASA) of the USA approved the continuation of operation of the FGRST space laboratory.

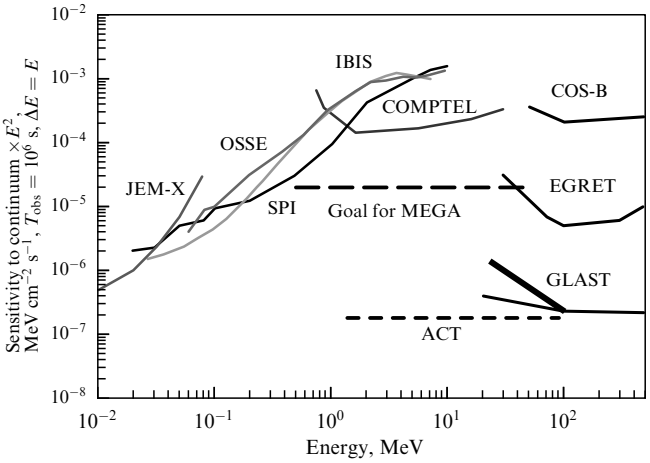

Figure 6. Curves of sensitivity of gamma-ray and X-ray telescopes, including expected sensitivity of the MEGA telescope [48].

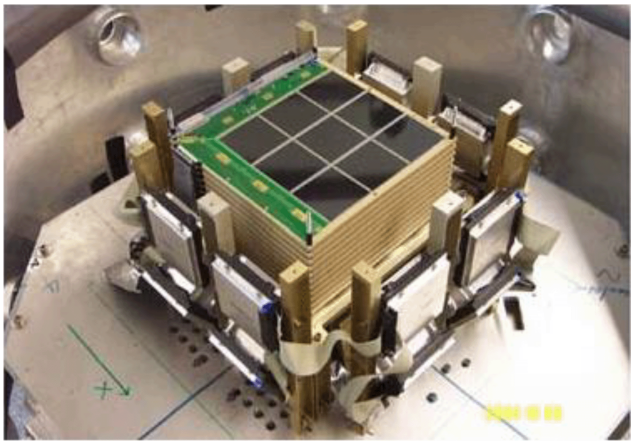

Figure 7. Prototype of the MEGA telescope with a layer of 3×3 DSSDs seen on top [48].

However, the range of gamma radiation energies from a few ten keV to a few hundred MeV remains largely unexplored since the time the first but limited observations on the COMPTEL telescope terminated in 2000. Therefore, this range is a special research objective in approaches for new space gamma-ray observatories proposed during the last 20 years, or observations in this range enter a wider range of energies. The purpose of these projects is to obtain data on the sources of gamma quanta at a new level of experimental capabilities. Further progress in the development of trackers used in gamma-ray telescopes is associated with the planned usage of silicon DSSDs. Below, examples of concepts of space gamma-ray observatories are presented with an emphasis on the description of trackers based on such detectors, whereas the scientific goals of the observatories are described in detail in the cited papers.

The concept of the Medium Energy Gamma-ray Astronomy (MEGA) space telescope, declared in 2002 [12], aims to view the entire sky in the range of medium energy gamma radiation (0.4–50 MeV), continuing studies in this interval after terminating operation of the COMPTEL with a sensitivity at least an order of magnitude higher than in the COMPTEL (Fig. 6). The telescope will be the first step in the creation of the Advanced Compton Telescope (ACT) observatory within the framework of the NASA program, where the sensitivity is planned to be increased by one more order of magnitude. The mid-energy range of gamma quanta is of particular importance for astrophysical problems, especially those related to nuclear, nonthermal, and relativistic processes. The scientific goals of MEGA are focused on composing an extended catalogue of gamma radiation sources in this range of energies; they are described in detail in Refs [12, 47–50]. The operation of the MEGA telescope is based on exploring Compton scattering (lower energies) and the creation of $e-e^+$ pairs for the energy of gamma quanta $E_\gamma > 10$ MeV. In both cases, the primary interaction creates secondary particles with long free paths, whose characteristics are used to reconstruct the propagation of the primary gamma quantum and the position of the source.

The telescope implies using two independent modules: a tracker, including DSSDs, in which the Compton scattering of an incident gamma quantum or conversion of its energy into $e-e^+$-pairs occurs, and a calorimeter based on pixel CsI detectors for absorption and measurement of the energy of secondary particles. For the telescope prototype (Fig. 7) at the Max Planck Institute for Extraterrestrial Physics (Garching, Germany), DSSDs based on n-Si wafers with a resistivity of ~ 10 kΩ cm, a thickness of 500 μm, and a strip pitch of 470 μm were developed. In the tracker, it was planned to use 10 layers with 3×3 DSSDs in each, and the calorimeter was planned to consist of 20 modules of CsI detectors, each of them being an assemblage of crystals with the dimensions 10×12 cm^2 and length of 2, 4, and 8 cm. It had p–i–n diodes at both ends, which allowed determining the depth of interaction of photons from the ratio of light yield at the ends. The capability of tracing electrons is the main advantage of the MEGA concept, since it allows decreasing the intensity of background events.

The calibration of the MEGA prototype using laboratory sources of ^{22}Na, ^{137}Cs, and ^{88}Y, carried out in 2003, showed that the prototype operates in a wide range of energies and the DSSD resolution in energy, position, and time is appropriate for the assigned tasks [48]. Good capabilities of visualizing sources of gamma quanta were demonstrated and further tests of the prototype were planned to investigate the methods of background suppression.

The space observatory project All-Sky-ASTROGAM, a MeV Companion for Multimessenger Astrophysics [51], is aimed at the problems of fast detection, localization, and gamma-ray spectroscopy of bursts and the merging of compact objects in the Universe with unprecedented sensitivity and polarimetric facilities with E_γ values in the range of a few MeV. It is based on the concept of the space gamma-ray observatory e-ASTROGAM (enhanced ASTROGAM) [13, 52, 53] for the study of nonthermal processes in the Universe in the range of $E_\gamma = 0.3$ MeV–3 GeV, within which the low limit of the range can be brought to 150 keV for the tracker and 30 keV for the calorimeter. In the ASTROMEV gamma-ray telescope [53] separated into a special unit, studies in the range from 100 MeV to 1 GeV are planned. The implementation of the e-ASTROGAM observatory can provide new data about nonthermal processes in astrophysical objects by carrying out observations of the highest-power galactic and extragalactic sources. The scientific goals, aspects of the exploration of processes related to gamma radiation, and the expected results based on simulations are thoroughly described in Refs [13, 53].

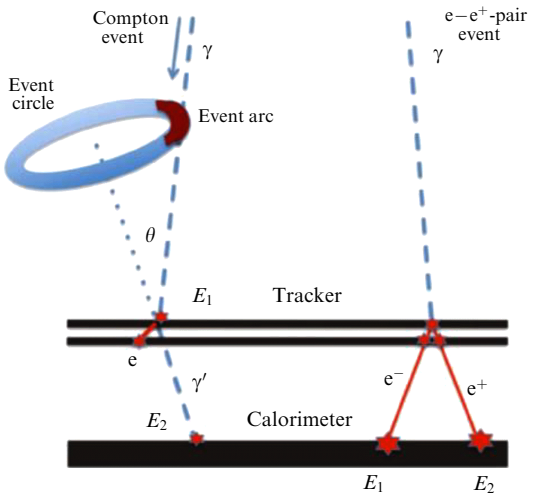

Figure 8. Illustration of Compton scattering events, formation of $e-e^+$ pairs, and reconstruction of the position of gamma quanta source in the e-ASTROGAM telescope; two DSSD layers of 56 layers forming the tracker and calorimeter are shown; blue dashed lines are tracks of gamma quanta; solid red lines are tracks of electrons and positrons [53].

The payload of e-ASTROGAM will consist of one gamma-ray telescope weighting 1.2 t, operating in the range of 150 keV–3 GeV. The recording instrumentation of the telescope is largely like that of the MEGA telescope. It includes a tracker consisting of 56 panels of DSSDs (the area of each panel is ~ 1 m^2) and a calorimeter for measuring the energy of the secondary particles, which is an array of CsI(Tl) rods, each having the dimensions of $5 \times 5 \times 80$ mm^3 and relative energy resolution of 4.5% for gamma quanta with an energy of 662 keV [53]. In addition, there is an anti-coincidence system based on standard scintillators, a time-of-flight (ToF) module with a time resolution of 300 ps designed to filter background radiation from the mechanical parts of the platform, modules of signal recording electronics, a data processing unit, and a power supply based on solar panels.

It is planned that the silicon tracker will detect charged particles — recoil electrons at $E_\gamma < 10$ MeV and $e-e^+$ pairs at E_γ in the range of a few GeV. It will include 5600 DSSDs arranged in 56 panels divided into four parts, 5×5 DSSDs in each, in which the strips are connected using the ultrasound welding technique to form a 2D array. Each DSSD will have a geometric area of 9.5×9.5 cm^2, thickness of 500 μm, and strip pitch of 240 μm. The total area of the detectors will amount to 90 m^2. Such assembling of detectors with a quite small thickness allows efficient tracing of the trajectories of recoil electrons and $e-e^+$ pairs. The signals of the DSSDs will be registered by low-noise electronics with 860,160 channels and possible internal synchronization. The calorimeter effectively absorbing gamma quanta is an array of 33,856 CsI(Tl) parallelepipeds 8 cm long with a cross section of 5×5 mm^2. The scintillations will be registered by silicon drift detectors located on both faces of the array in the form of a matrix of 529 (23×23) elementary modules with 64 crystals in each.

Figure 8 illustrates the events of Compton scattering and the creation of $e-e^+$ pairs in the registering instrumentation of the telescope [53]. Blue dashed lines show the tracks of gamma quanta absorbed in the tracker and the calorimeter; solid red lines represent the tracks of electrons and positrons. The step-by-step procedure for processing the data on energy deposition and the tracks of electrons allows first determining the event circle of the registered gamma quanta and then selecting the event arc.

The requirements with regard to the characteristics of the e-ASTROGAM and ASTROMEV observatories are presented in Refs [13, 52, 53]. Estimates of the expected characteristics of the observatory, obtained by detailed simulation of its operation, are [53]:

- energy range of the detected gamma quanta is 0.15 MeV–3 GeV with the sensitivity at $E_\gamma = 0.3-100$ MeV improved by almost two orders of magnitude compared to the COMPTEL telescope (Fig. 9);
- unprecedentedly high angular resolution in the region of units of MeV and above a few hundred MeV, exceeding the results from COMPTEL and Fermi-LAT by nearly 4 times at the energy of gamma quanta of 5 MeV and 1 GeV, respectively (Fig. 10);
- new level of polarimetric facilities for both stationary and nonstationary sources.

The concept of the All-sky Medium Energy Gamma-ray Observatory (AMEGO) combines high sensitivity in the energy range of 200 keV–10 GeV with a wide field of view, high spectral resolution, and polarization sensitivity [54–58]. The scientific instrumentation of the observatory will include

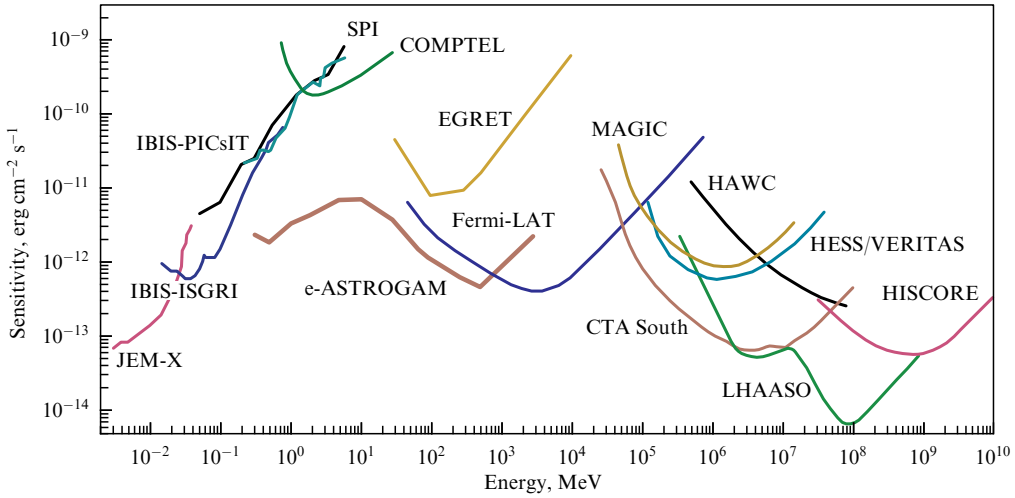

Figure 9. Differential sensitivity of X-ray and gamma-ray telescopes and expected result for the e-ASTROGAM telescope [53].

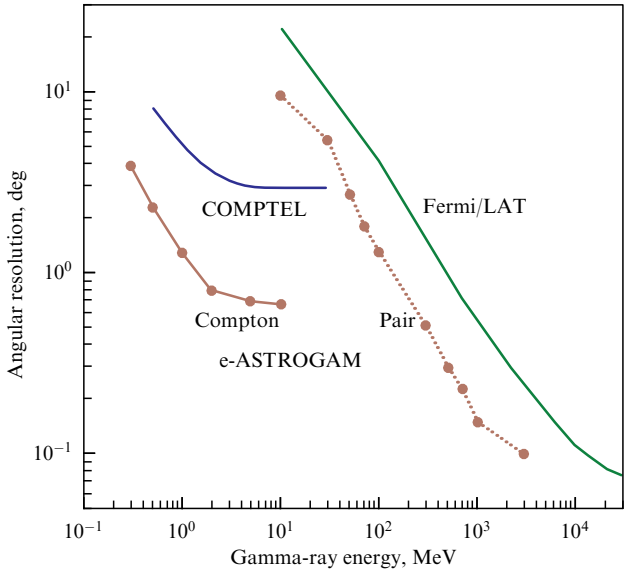

Figure 10. Angular resolution of e-ASTROGAM, COMPTEL, and Fermi-LAT telescopes.

a tracker based on DSSDs, two calorimeters, as well as an anticoincidence system [55, 57]. The silicon tracker is divided into 4 module assemblies, each consisting of 60 layers of DSSDs. A calorimeter based on the CZT (Cd-Zn-Te) is directly under the tracker when detecting Compton events, whereas the CsI calorimeter has a thickness sufficient to detect $e-e^+$ pairs to extend the range of energies to 10 GeV. For the preliminary testing of the tracker detectors, DSSDs produced by Micron Semiconductors, Great Britain, will be used. Each detector is a square with each side being 10 cm and a thickness of 500 μm, having on each side 192 strips with a pitch and width of $\sim$ 510 μm and 60 μm, respectively.

Thus, the AMEGO concept is based on the rich heritage of the Fermi-LAT telescope and innovative technologies developed for detectors of gamma radiation and cosmic rays which will make it possible to obtain more precise data in an extended range of energies from $\sim$ 300 keV to more than 10 GeV, thanks to, among other things, a more than 20-fold improvement in sensitivity compared to the results of COMPTEL in the overlapping range of energies [54].

In conclusion, it should be noted that the successful functioning of the FGRST observatory for already almost 20 years proves the high reliability of the research instrumentation, including the silicon trackers.

4. Prospects for creating space gamma-ray observatories in Russia

The potential of Russia, including Ioffe Institute, to participate in the creation and operation of space observatories to investigate gamma radiation has two aspects. The first is the participation of Ioffe Institute specialists in multidisciplinary fundamental studies of cosmic radiation in the Universe, carried out within the framework of international collaborations. Here, we should mention the Payload for Antimatter-Matter Exploration and Light-Nuclei Astrophysics (PAMELA) space observatory [59–61], intended to register light charged particles in the cosmic radiation with energies from hundreds of MeV to TeV to detect the 'dark' matter and antimatter in space. The recording instruments of the observatory included an electromagnetic calorimeter consisting of 44 layers of SSSDs. The data collected during 10 years of operation allowed obtaining new results on the composition of cosmic radiation and the effect of solar activity on it. In addition, the belt of antiprotons surrounding Earth was recorded for the first time.

Another example is fundamental research on cosmic gamma bursts, the history and results of which are presented in Refs [62, 63]. Starting from the mid-1960s, such studies were carried out by specialists of the Ioffe Institute on spacecraft of the Kosmos series and Venera stations. For the latter, the high-sensitivity Konus research instrument was manufactured based on scintillation detectors. Later, the studies were continued within the Konus-Wind international experiment and the HELICON experiment of the Ioffe Institute: the equipment was located at a distance of 200 km from Earth, and in 2004 this made it possible to detect the reflection from the Moon of a giant flare of gamma quanta with an energy of 2.3×10^{46} erg [64].

The second aspect is that Ioffe Institute researchers have for more than 20 years taken part in the development and research on silicon detectors. This is related to work on the LHC in the ROSE, RD39, and RD50 collaborations at CERN [65–71] aimed at improving the radiation hardness of detectors. It is also necessary to note the contribution to the physical studies of silicon detectors within the program of creating an inner tracker of the CERN-ATLAS experiment [72, 73], the development of the concept and manufacturing of detectors for the CERN-TOTEM experiment [74], and the participation in the pilot project of CERN on the development of silicon cryogenic monitors of a proton beam for the LHC [75]. During the last 10 years, several projects have been carried out in collaboration with the GSI center (CBM and EXL experiments and collaboration for development of ToF diagnostics of ions for the ion separator at GSI) [22, 76–79] and the Joint Institute for Nuclear Research (Dubna) [80]. In the field of developing and manufacturing silicon detectors for HEP and nuclear physics problems, the Ioffe Institute has for many years collaborated with technological organizations in Zelenograd. All this determines the competence and potentialities of the institute in solving the problems of creating silicon detectors and devices based on them.

One more area of study developed by the Ioffe Institute is the design of electronic devices for recording radiation for Cherenkov telescopes and position-sensitive segmented silicon detectors [81–85]. To master the technology for creating cameras for Cherenkov gamma-ray telescopes of the fourth generation (in particular, within the ALEGRO project [81]) and increasing the efficiency of operation of existing Cherenkov gamma-ray observatories, a detector cluster based on SiPM-type photodetectors for operating the TAIGA-IACT Cherenkov telescope is being developed at the institute [85].

The Ioffe Institute's competencies in the research and development of silicon detectors include the following:

(1) Semiconductor detector physics:

- modeling the characteristics of silicon detectors and optimizing their structure and conditions of operation [68, 69, 86–94];
- physical substantiation of silicon detector design [74, 88, 95–98];
- studies of radiation impact on the detectors and modeling the scenario of radiation degradation under standard conditions [37, 94, 95, 99–104];

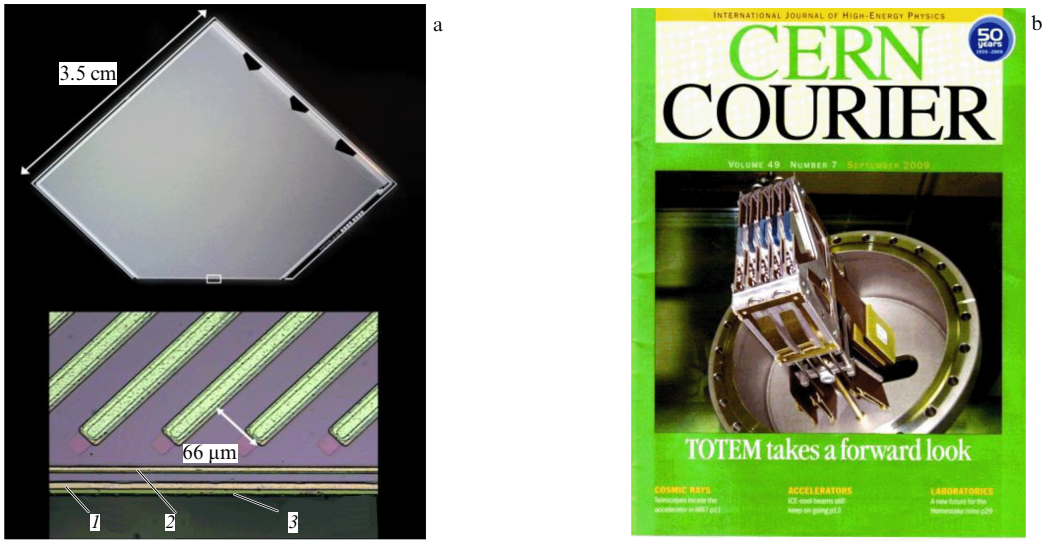

Figure 11. 'Edgeless' detectors for TOTEM experiment: (a) silicon detector chip with a microphotograph of its sensitive edge [96], *1* — current-restricting ring, *2* — guard ring, *3* — sensitive edge; (b) assemblage of detectors installed on a flange.

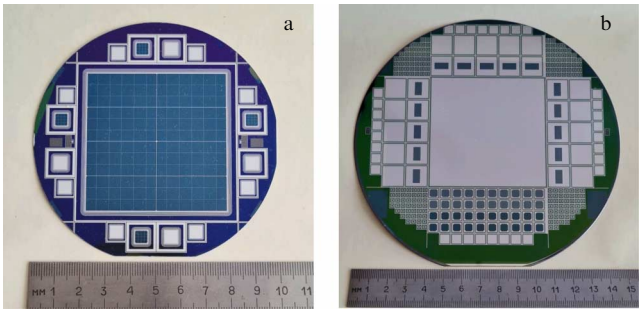

Figure 12. Planar segmented silicon detectors: (a) 2 × 4 pixel detector of ions with dimensions of 60 × 60 mm^2 for experiments in the FAIR program; wafer diameter is 100 mm; (b) detectors of various types, including SSSD in the center; the wafer diameter is 150 mm.

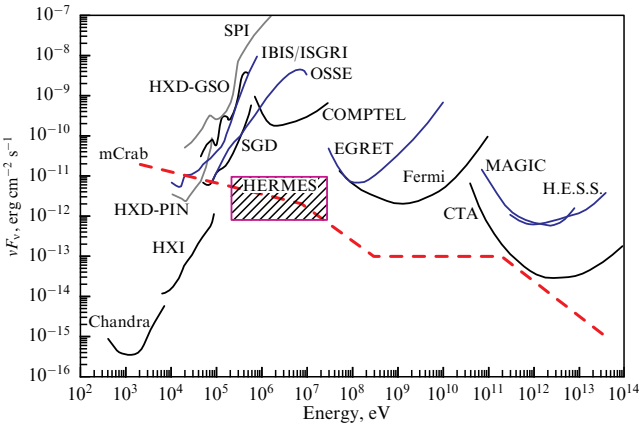

Figure 13. Sensitivity of gamma-ray telescopes. Red line shows energy flux corresponding to the level of 10^{-3} of the value characteristic of the Crab Nebula [14].

• studies of radiation degradation of detectors under cryogenic conditions down to a temperature of 1.9 K [75, 105–111];

• studies of signal formation in segmented detectors [22, 23, 80, 92, 111–114].

(2) Development and supply of silicon detectors:

• silicon mini-detectors for studies within the research programs of the CERN-RD39 and CERN-RD50 collaborations (1997–2022);

• a complete set of 'edgeless' detectors for the CERN-TOTEM experiment (2005–2007); 400 detectors are still successfully being used in the experiment [115];

• prototypes of particle loss monitors for the LHC proton beam for operation at 1.9 K (2012–2015) [116];

• pilot run of spectrometric DSSDs, the FAIR program, the NuSTAR-EXL experiment, GSI (2007–2010);

• test samples of spectrometric DSSDs for ToF measurements with a time resolution of < 50 ps, the FAIR program, Surep-FRS (2015–2017, 2021–2022) [22].

Examples of silicon detectors developed and manufactured for LHC and GSI experiments are illustrated in Figs 11 and 12. Note that the 'edgeless' DSSDs for the TOTEM experiment aimed at measuring the low angle scattering of protons upon a collision of their intersecting beams possess a uniquely small 'dead' zone between the strips and the edge of the detector chip, amounting to ~ 45 μm [74, 96]. In this case, the dark currents and the range of operating voltages of the detectors before irradiation had the same values as in conventional DSSDs.

The Ioffe Institute's potential in the field of gamma-ray astrophysics and the development of detecting devices is planned to be concentrated within the HERMES gamma-ray telescope project [14], oriented at problems with nuclear spectroscopy, in which it is relevant to detect gamma quanta in the energy range of 0.3–10 MeV. To date, the maximal sensitivity of measurements in the above range has been reached with COMPTEL, equipped with a scintillation detector. Figure 13 also shows the sensitivity level for the silicon tracker in the proposed HERMES telescope. In addition, the restriction of the range of studied energy of gamma quanta to 10 MeV allows abandoning the calorimeter and thus improving the weight characteristic of the telescope.

As follows from Section 3, the creation of trackers based on silicon detectors for gamma-ray telescopes in recent years is the same large-scale task as the creation of an instrument base for LHC experiments. The possibility of implementing the required characteristics of the tracker in the HERMES

Table 2. Characteristics of DSSDs planned for the tracker of e-ASTROGAM telescope and strip detectors developed at the Ioffe Institute.

Characteristics	e-ASTROGAM [13]	Ioffe Institute
Sensitive region thickness, μm	500	300–1000
Operating voltage, V	up to 400	400
Detector area, cm^2	9.5×9.5	10×10
Strip pitch, μm	240	500–1000
Strip current at 0 °C, nA mm^{-2}	0.007	0.004

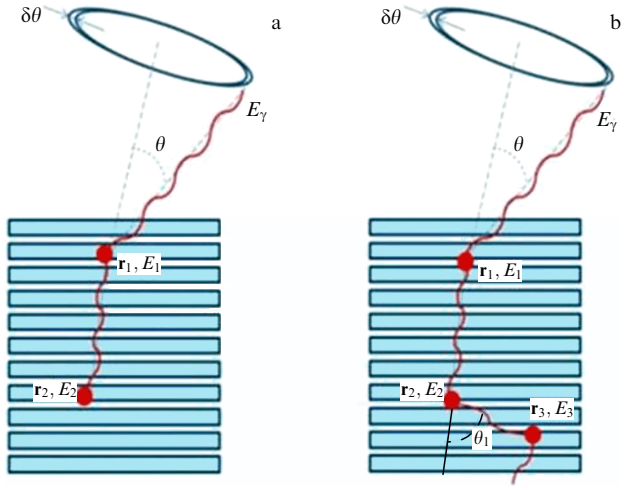

Figure 14. Compton process of gamma quantum registration in a silicon tracker: (a) two-stage process with full absorption of quantum energy, (b) three-stage process with partial absorption of quantum energy; **r** is the vector that determines the point where the Compton event occurred.

observatory is illustrated in Table 2, where a comparison is made of the structure parameters used in the sensor topology developed by Ioffe Institute specialists and the parameters of DSSDs planned for the e-ASTROGAM space observatory.

Solving the problem of creating silicon detectors for trackers requires an approach that considers the specifics of gamma quanta absorption in silicon. The process of gamma quantum detection, in which the quantum energy is determined and the direction of its motion to the tracker is reconstructed, is illustrated in Fig. 14. The gamma quantum incident on the detector surface at angle θ with energy E_γ undergoes Compton scattering on an electron at some point in one of the silicon detectors of the tracker, producing a recoil electron with energy E_1 and decreasing its own energy to $E_\gamma - E_1$. The scattered gamma quantum continuing its motion in a new direction has a probability of being scattered by an electron at another point of the tracker, transferring to the electron energy E_2 and, correspondingly, once more changing the energy and the direction of motion. The expression relating θ to the energy losses E_1 and E_2 allows determining the angle of incidence of the gamma quantum on the detector:

$$\cos\theta = 1 - m_e c^2 \left(\frac{1}{E_2} - \frac{1}{E_1 + E_2} \right), \qquad (10)$$

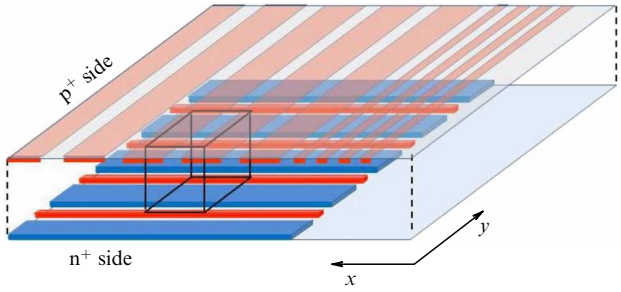

Figure 15. Schematic view of a DSSD. Strips on p^+ and n^+ sides are shown in light brown and blue, respectively; red elements on n^+ side in the interstrip gaps are the p^+ isolation. The sensitive cell volume is shown as a parallelepiped.

where $m_e c^2 = 511$ keV is the rest energy of an electron. Thus, in the tracker, the conditions should be implemented for at least a twofold interaction of the quantum with electrons and determination of 3D coordinates of the points of formation of recoil electrons and their energy.

Note that silicon is the preferred material in terms of the influence of the Doppler effect on the resolution, which is proportional to the value of Z.

Thus, the optimal detector for registering the recoil electrons should be an array of volume sensitive cells, in which the creation of an electron will always yield a standard set of data, i.e., three coordinates of the point of electron creation and its energy. Based on the constructions of the detectors described in Section 2, such an opportunity can be implemented in the structure of a pixel detector or DSSD; the latter is schematically shown in Fig. 15. It should be noted that the pixel detector possesses a maximum rate of particle detection and provides unambiguous information about the site of detection of each particle. The main disadvantage noted above is the large number of parallel channels of electronics required to record the signals, equal to $A_x \times A_y$. The use of DSSDs provides economy in the number of electronic channels, which becomes $A_x + A_y$; however, in this case, the maximum rate of particle detection decreases, which leads to a loss of events occurring. However, at a low intensity of radiation, expected in the HERMES experiment, the savings in the number of electronic channels argues for the use of DSSDs. Such a detector is shown in Fig. 15. It is made of a wafer of n-Si, on the upper and lower sides of which orthogonal arrays of p^+ and n^+ strips are created, respectively. The strips on the upper side form $p^+ - n$ junctions, separated by a gap covered with an isolating layer of SiO_2. A similar separation is executed on the n^+ side with the addition of p^+ isolating elements between the strips. The sensitive cells, one of which is shown by black lines, are formed at the place of crossing of orthogonal strip projections.

The description of DSSDs would be incomplete without presenting two important elements, the VTS at the side of p^+ strips and p^+ isolation in the interstrip gaps on the n^+ side. It is exactly these elements that determine the stability of the DSSD static characteristics and the range of possible operating voltages. The VTS structure is used in practically all types of planar detectors and allows optimization of the distribution of the electric field at the periphery of the detector operating region, avoiding electric breakdown. Figure 16 presents a sectional view of the detector with the VTS, which is a sequence of isolated p^+ rings located around the p^+ region of the main junction to which the operating

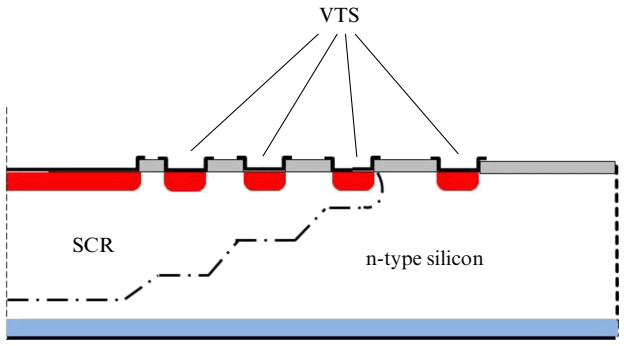

Figure 16. VTS structure on p^+ side of a detector with four rings of similar width and different width of gaps between rings. Dashed-dotted line shows SCR boundary at the voltage applied to the detector and activating only three VTS rings.

voltage is applied, while the lower n^+ side of the detector is grounded. Without a VTS structure, all the voltage between p^+ and n^+ contacts would be applied to the boundary of the main junction, where a local region with an increased electric field would arise. In the literature, several methods of controlling the electric field at the boundary of the p^+-n junction are described, including by mechanical profiling (e.g., making a bevel), which is not matched with the operations of planar technology. Therefore, the creation of a VTS, including isolated p^+ rings, is generally accepted for planar detectors and is formed in a single technological process of manufacturing the entire detector. The functioning of the VTS is based on the regularities of potential distribution between isolated p^+-n junctions placed at some distance from each other [93, 94, 117, 118]. In such a system of junctions, the potential from the main p^+-n junction is transferred to isolated junctions at the closing of the boundaries of individual regions of space charge. In this case, conditions are created for current flowing between p^+ regions and the creation of a common SCR (Fig. 16).

The closing of boundaries between adjacent p^+-n junctions is a formal explanation of the electric field propagation effect in VTS. It is necessary to comment here that the boundary of the SCR junction is always blurred due to diffusion and drift processes that control the distribution of concentrations of free electrons and holes. This depends not only on the profile of doping the p^+ regions but also on the charge in the oxide between them. Since the charge in the SiO_2 layer is positive, the motion of holes under the Si–SiO_2 interface is interrupted; the greater the charge, the higher the difference in potentials between the rings necessary for current flowing and joining the SCRs of adjacent rings. Such a state of a VTS is shown in Fig. 16, where the SCR joins three rings, and its boundary (dashed-dotted) has a stepped character due to different potentials established on individual rings. The merging of the SCR of the fourth ring with those of the first three rings requires applying even higher voltage to the main junction. The current magnitudes between the p^+ regions joining the rings into a united system are determined by the dark currents generated in the sensitive region of the detector and lie in the range from pA to tens of nA, which imposes strict requirements on VTS.

It is important to note that the condition for starting up and maintaining the current coupling between the rings depends not only on the condition of the oxide but also on the electric field component in the region of the gap between

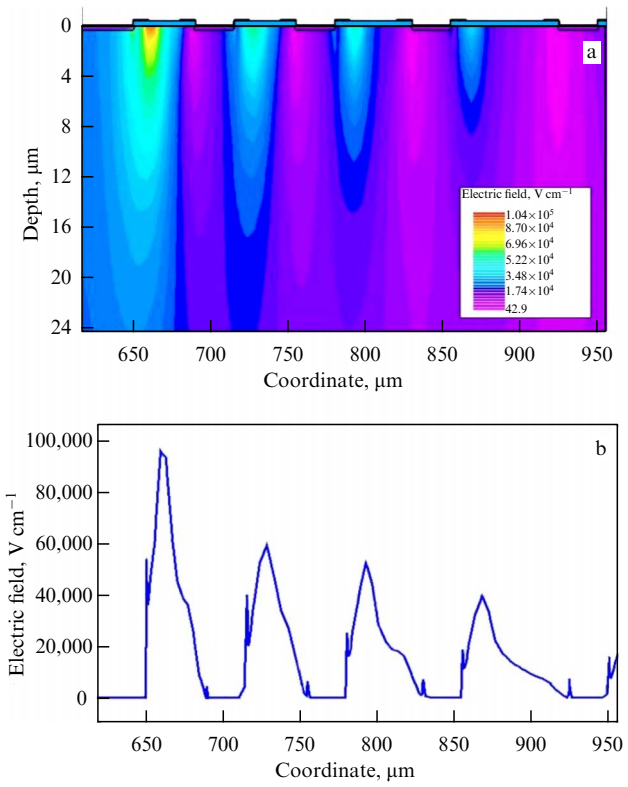

Figure 17. Some of the calculated electric field distribution in the region of four VTS rings at $V = 500$ V; main p^+-n junction is located on the left: (a) 2D distribution of the electric field, (b) electric field profile at a depth of 0.6 μm.

the rings, perpendicular to the surface of the p side of the detector and depending on the voltage. Despite the significant number of parameters, the system of the above processes is stabilized by the condition of opening the above current channel between the rings for the drift of holes, which determines the distribution of potential over the rings and electric fields at all points of the SCR at any voltage. Of practical importance is that the setting of the potential on the rings occurs automatically and for a correctly designed VTS is characterized by a sequential decrease in its value from the maximum at the central p^+ electrode to zero on the last ring.

The task of VTS modeling and optimization required solving a system of equations describing the static distribution of the electric field and currents in the detector volume. For this, professional software packages are used that model the entire set of basic processes in p–i–n structures, i.e., generation, recombination, drift, and diffusion of electrons and holes, distribution of dopant impurities, processes at interfaces, etc., in quantitative 2D and 3D detector models. As an example, we present below the results of 2D simulation of the operation of critical elements of DSSDs, including VTS and p^+ isolation of n^+ strips.

Figure 17a shows the results of modeling a 2D distribution of the electric field in the VTS of a silicon detector at $V = 500$ V. The distribution is characterized by electric field maxima in the regions of the outer borders of the ring metal films deposited on the SiO_2 layer. Their values decrease as the ring becomes farther from the main p^+-n junction (Fig. 17b), and the maximum value at the boundary of the sensitive region does not exceed 10^5 V cm^{-1} (red area in Fig. 17a), which is one half or even less than the values at which the

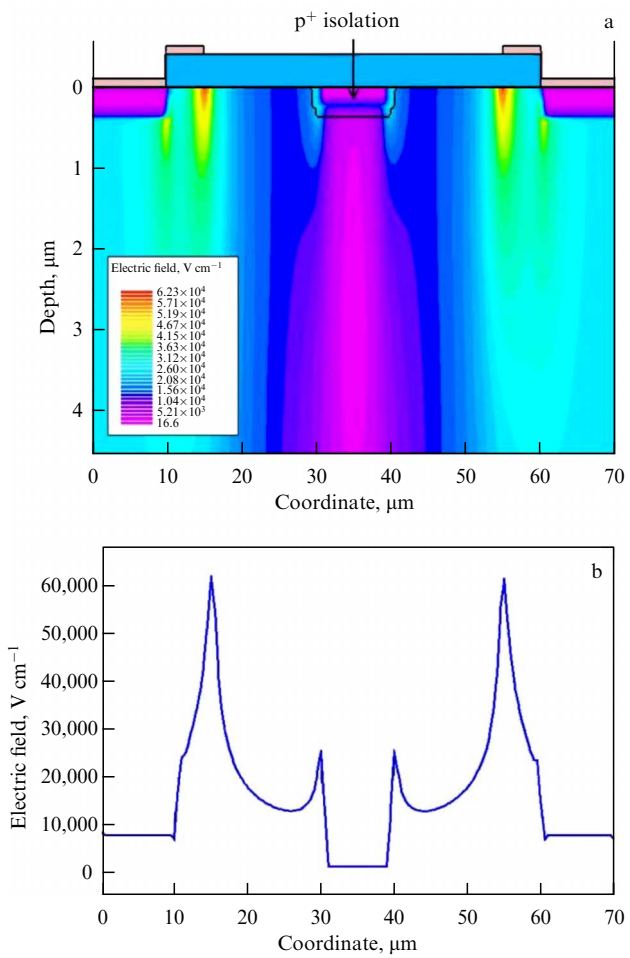

Figure 18. Part of calculated electric field distribution in the section of the interstrip gap with interstrip p^+ isolation on the n^+ side of the detector: (a) 2D distribution of the electric field, (b) electric field profile at a depth of 0.6 μm. $V = 500$ V.

electric breakdown due to impact ionization is possible. We should note that the modeling of the electric field is carried out in the 2D space, when the ring boundaries and profiles of doping are smooth, i.e., the inhomogeneities in the direction of the axis perpendicular to the structure section surface are absent.

The second critical DSSD element is the interstrip isolation of the segmented n^+ contact of the detector. For this contact, the above simple segmentation, by analogy with p^+ strips, does not provide electric isolation of strips due to the built-in positive charge in SiO_2 located in the gap between the n^+ strips, which gives rise to a layer of accumulated electrons under the SiO_2. This layer electrically connects adjacent n^+ contacts, forming a single nonsegmented n^+ contact. An effective solution to the problem is to surround each n^+ strip with a p^+ ring (similar to the n^+-p-p^+ detector) or create a general p^+ grid on the n side, in the cells of which n^+ strips are located.

Applying voltage to the detector causes an outflow of holes from this p^+ element of interstrip isolation, due to which it acquires a potential different from the potential of n^+ strips by tens and for nonoptimal construction by hundreds of volts. Figures 18a and b present the results of modeling the electric field between n^+ strips isolated by a p^+ element. It is seen that the outflow of holes from the p^+ isolating structure causes substantial specific features in the distribution of the field in the interstrip gap. Under the p^+ element, a region with a minimum electric field arises that breaks the connection between the adjacent strips. In this case, the difference in potentials between the p^+ element and the neighboring n^+ strips turns out to be substantial, which follows from the value of the field maximum of $\sim 6 \times 10^4$ V cm^{-1}. As in the distributions on the p^+ side of the detector, such maxima are localized near the boundary of the strip metallization (red area in Fig. 18a).

The above results of the numerical modeling of DSSD critical elements show that, in the VTS and interstrip isolation of n^+ strips, the maximum field arises at the boundary of metallization, located on the SiO_2 layer. At $V = 500$ V, the maximum field magnitude in the peaks amounts to 1×10^5 and 6×10^4 V cm^{-1} for the p and n side, respectively, which is lower than the field strength initiating an avalanche breakdown. Note that the real electric field in critical elements of the fabricated detector depends on the characteristics of the silicon that forms the sensitive volume, the presence of defects in it, the properties of the oxide, and the precision of photolithography structuring the boundaries of the doped regions, the SiO_2 layer, and the metal. From the practical point of view, the obtained result should be considered an estimate of the ideal detector characteristics, since any sharp bumps at the metallization boundary (extended defects in the silicon volume, defects of photolithography, etc.) can multiply enhance the effect of field focusing on thin p^+ and n^+ layers [73, 113] and lead to instabilities and breakdown effects. This remark is important for designing complex structures of detectors, to which DSSDs belong, with the total length of the boundaries of elements reaching 60 meters (DSSDs measuring 10×10 cm^2 with the number of strips equal to 100 on each side).

5. Conclusions

The development stages of the instrumental base of gamma-ray astronomy are similar to those in the development of the HEP instrumental base. New ideas for HEP that required experimental data at a qualitatively new level upon increasing the energy of particles and intensity of their beams stimulated the creation of new detecting devices, including universal silicon detectors and devices based on them. The most striking results were the work at the LHC at CERN, in which the experimental base was thoroughly approved by the international scientific society and the unique fundamental results, e.g., the discovery of the Higgs boson. A similar process takes place in experimental astrophysics, where gamma-ray telescopes based on scintillation detectors are no longer appropriate for new fundamental problems in sensitivity and angular resolution. To create new gamma-ray telescopes, it is planned to change to silicon detectors that allow creating a 3D recording medium with a volume of up to 1 m^3 sensitive to gamma quanta and providing the $3D + t$ information needed to determine the position of their source in the Universe. These problems can be solved based on the accumulated experience in exploiting the already existing types of silicon detectors and technologies of their large-batch production.

The presented review allows concluding that at present there is no fundamental limitation on the characteristics of the developed space gamma-ray telescopes. The limitations are largely due to the level of financing and the carrier

facilities for launching the telescope into orbit. In this connection, the HERMES project mentioned above belongs to a special research task aimed at the energy range from hundreds of keV to 10 MeV, in which gamma quanta interact with silicon mainly via Compton scattering and, therefore, the telescope construction required no massive calorimeter or time-of-flight detector, which substantially reduces the telescope weight, its cost, and launch expenditures.

The detecting medium of such a telescope is based optimally on silicon DSSDs. For guaranteed stable operation of DSSDs in space, detailed modeling of the design of their critical elements is required at the development stage. The presented characteristics of the DSSD prototypes for the planned e-ASTROGAM and HERMES observatories show the reality of creating modern gamma-ray telescopes in Russia based on the experience in studies of cosmic radiation, the physics of semiconductor detectors, and the existing technological base for developing silicon detectors.

The research on and development of silicon detectors were supported by the Russian Foundation for Basic Research, grant no. 05-02-08337ofi_a, the Presidium of the Russian Academy of Sciences within the programs Experimental and Theoretical Studies of Fundamental Interactions Related to Work at the CERN Accelerating Facility and High-Energy Physics and Neutrino Astrophysics, CERN-INTAS, grant nos 99-850, 03-52-5744, 05-103-7533, and GSI-INTAS, grant no. 06-1000012-8844.

References

1. Lutz G *Semiconductor Radiation Detectors*: *Device Physics* (Berlin: Springer-Verlag, 1999); Lutz G *Semiconductor Radiation Detectors*: *Device Physics* (Berlin: Springer-Verlag, 2007) https://doi.org/10.1007/978-3-540-71679-2
2. Fabjan C W, Schopper H (Eds) *Particle Physics Reference Library* Vol. 2 *Detectors for Particles and Radiation* (Berlin: Springer, 2011)
3. Akimov Yu K *Poluprovodnikovye Detektory Yadernykh Izluchenii* (Semiconductor Detectors of Nuclear Radiation) (Dubna: JINR, 2009)
4. Knoll G F *Radiation Detection and Measurement* 4th ed. (Hoboken, NJ: John Wiley, 2010)
5. Béjar A I et al. (Eds) "High-Luminosity Large Hadron Collider (HL-LHC)," Technical Design Report (CERN Yellow Reports: Monographs, CERN-2020-010) (Geneva: CERN, 2020) https://doi.org/10.23731/CYRM-2020-0010
6. Moll M *IEEE Trans. Nucl. Sci.* **65** 1561 (2018)
7. Hartmann F (ATLAS, ALICE, CMS, LHCb Collab.) *Nucl. Instrum. Meth. Phys. Res. A* **924** 250 (2019)
8. Szumlak T (RD50 Collab.) *Nucl. Instrum. Meth. Phys. Res. A* **958** 162187 (2020)
9. Dalla Betta G-F, Ye J "Silicon radiation detector technologies: from planar to 3D" *Chips* **2** (2) 83 (2023)
10. Schönfelder V et al. *Astrophys. J. Suppl.* **86** 657 (1993)
11. Atwood W B et al. *Astrophys. J.* **697** 1071 (2009)
12. Bloser P F et al. (MEGA Collab.) *New Astron. Rev.* **46** 611 (2002)
13. De Angelis A et al. *J. High Energy Astrophys.* **19** 1 (2018)
14. Krassilchtchikov A M et al. *J. Phys. Conf. Ser.* **1400** 022031 (2019)
15. Sze S M, Ng K K *Physics of Semiconductor Devices* 3rd ed. (Hoboken, NJ, USA: Wiley, 2007) https://doi.org/10.1002/0470068329
16. Ramo S *Proc. IRE* **27** 584 (1939)
17. Jacoboni C et al. *Solid-State Electron.* **20** 77 (1977)
18. Affolder A (ATLAS Collab.) *Phys. Procedia* **37** 915 (2012)
19. Unno Y et al. *Nucl. Instrum. Meth. Phys. Res. A* **731** 183 (2013)
20. Unno Y et al. *Nucl. Instrum. Meth. Phys. Res. A* **765** 80 (2014)
21. Pellegrini G et al. *Nucl. Instrum. Meth. Phys. Res. A* **566** 360 (2006)
22. Kiselev O A et al., in *Exotic Nuclei. Proc. of the Intern. Symp. on Exotic Nuclei, EXON-2014, Kaliningrad, Russia, 8–13 September 2014* (Eds Yu E Penionzhkevich, Yu G Sobolev) (Singapore: World Scientific, 2015) p. 607, https://doi.org/10.1142/9789814699464_0061
23. Eremin V et al. *Nucl. Instrum. Meth. Phys. Res. A* **796** 158 (2015)
24. Nakamura K et al. *JINST* **10** C06008 (2015)
25. Ostrowski A N et al. *Nucl. Instrum. Meth. Phys. Res. A* **480** 448 (2002)
26. Takeda S et al. *Nucl. Instrum. Meth. Phys. Res. A* **579** 859 (2007)
27. Pellegrini G et al. *Nucl. Instrum. Meth. Phys. Res. A* **765** 12 (2014)
28. Pellegrini G et al. *Nucl. Instrum. Meth. Phys. Res. A* **831** 24 (2016)
29. Kramberger G et al. *Nucl. Instrum. Meth. Phys. Res. A* **891** 68 (2018)
30. Kramberger G et al. *Nucl. Instrum. Meth. Phys. Res. A* **898** 53 (2018)
31. Carulla M et al. *Nucl. Instrum. Meth. Phys. Res. A* **924** 373 (2019)
32. Parker S I, Kenney C J, Segal J *Nucl. Instrum. Meth. Phys. Res. A* **395** 328 (1997)
33. Kenney C et al. *IEEE Trans. Nucl. Sci.* **46** 1224 (1999)
34. Fleta C et al. *Nucl. Instrum. Meth. Phys. Res. A* **579** 642 (2007)
35. Pellegrini G et al. *Nucl. Instrum. Meth. Phys. Res. A* **592** 38 (2008)
36. Dalla Betta G-F et al. *Nucl. Instrum. Meth. Phys. Res. A* **624** 459 (2010)
37. Eremin V, Verbitskaya E, Li Z *Nucl. Instrum. Meth. Phys. Res. A* **476** 537 (2002)
38. Lindström G, Moll M, Fretwurst E *Nucl. Instrum. Meth. Phys. Res. A* **426** 1 (1999)
39. Kramberger G et al. *Nucl. Instrum. Meth. Phys. Res. A* **481** 297 (2002)
40. Grieder P K F "Ch. 5. Primary Cosmic Radiation," in *Cosmic Rays at Earth. Researcher's Reference Manual and Data Book* (Amsterdam: Elsevier, 2001) p. 669
41. Holder J et al. *Astropart. Phys.* **25** 391 (2006)
42. Coleman A et al. *Astropart. Phys.* **149** 102819 (2023)
43. Kholupenko E E et al. *Tech. Phys.* **65** 886 (2020); *Zh. Tekh. Fiz.* **90** 925 (2020) http://dx.doi.org/10.21883/JTF.2020.06.49278.354-19
44. Bykov A, Bloemen H *Astron. Astrophys.* **283** L1 (1994)
45. Schönfelder V et al. *Astron. Astrophys. Suppl. Ser.* **143** 145 (2000)
46. Atwood W B et al. *Astropart. Phys.* **28** 422 (2007)
47. Kanbach G et al. *New Astron. Rev.* **48** 275 (2004)
48. Bloser P F et al. *Chin. J. Astron. Astrophys.* **6** 388 (2006)
49. Bloser P F et al. *New Astron. Rev.* **50** 619 (2006)
50. Zoglauer A et al. *New Astron. Rev.* **50** 624 (2006)
51. De Angelis A et al. *PoS* **ICRC2019** 579 (2019)
52. The e-ASTROGAM Collab., De Angelis A et al. *Exp. Astron.* **44** 25 (2017)
53. De Angelis A et al. *Exp. Astron.* **51** 1225 (2021)
54. Moiseev A (AMEGO Team) *PoS* **ICRC2017** 798 (2017)
55. Caputo R, Kislat F, Racusin J *PoS* **ICRC2017** 783 (2017)
56. Orlando E et al. *PoS* **ICRC2019** 590 (2019)
57. Griffin S (AMEGO Team), arXiv:1902.09380
58. McEnery J E et al., arXiv:1907.07558
59. Boezio M et al. *Hyperfine Interact.* **213** 147 (2012)
60. Mori N et al. *Nucl. Part. Phys. Proc.* **265–266** 242 (2015)
61. Galper A M et al. *J. Phys. Conf. Ser.* **798** 012033 (2017)
62. Aptekar R L et al. *PoS* **GRB2012** 118 (2012)
63. Aptekar R L et al. *Phys. Usp.* **62** 739 (2019); *Usp. Fiz. Nauk* **189** 785 (2019)
64. Mazets E P et al. *Astrophys. J.* **680** 545 (2008)
65. Lindström G et al. *Nucl. Instrum. Meth. Phys. Res. A* **465** 60 (2001)
66. Casagrande L et al. *Nucl. Instrum. Meth. Phys. Res. A* **461** 150 (2001)
67. Collins P et al. *Nucl. Instrum. Meth. Phys. Res. A* **447** 151 (2000)
68. Niinikoski T O et al. *Nucl. Instrum. Meth. Phys. Res. A* **520** 87 (2004)
69. Li Z et al. *Nucl. Instrum. Meth. Phys. Res. A* **718** 266 (2013)
70. Moll M, RD50 Collab. *Nucl. Instrum. Meth. Phys. Res. A* **511** 97 (2003)
71. Affolder A et al. *PoS* **Vertex2013** 26 (2013)
72. Eremin V, Li Z, Iljashenko I *Nucl. Instrum. Meth. Phys. Res. A* **360** 458 (1995)
73. Eremin V et al. *Nucl. Instrum. Meth. Phys. Res. A* **535** 622 (2004)
74. Ruggiero G, Eremin V, Noschis E *Nucl. Instrum. Meth. Phys. Res. A* **582** 854 (2007)
75. Bartosik M R et al., CERN-BE-2014-009 BI (Geneva: CERN, 2014)
76. Ablyazimov T et al. *Eur. Phys. J. A* **53** 60 (2017)
77. Zamora J C et al. *Phys. Rev. C* **96** 034617 (2017)

78. Kiselev O et al., GSI Scientific Report GSI-SR2012-PHN-ENNA-EXP-42172 (Darmstadt: GSI Helmholtzzentrum für Schwerionenforschung GmbH, 2012)
79. Kostyleva D et al. *Acta Phys. Polon. B* **49** 503 (2018)
80. Eremin V et al. *JINST* **12** C03001 (2017)
81. Bykov A M et al. *Tech. Phys.* **62** 819 (2017); *Zh. Tekh. Fiz.* **87** 803 (2017)
82. Kholupenko E E et al. *Phys. Atom. Nucl.* **79** 1542 (2016); Translated from Russian: *Yad. Fiz. Inzhiniring* **7** (1) 37 (2016)
83. Bogdanov A A et al. *J. Phys. Conf. Ser.* **1400** 055050 (2019)
84. Tuboltsev Y V et al. *Instrum. Exp. Tech.* **62** 764 (2019); *Prib. Tekh. Eksp.* (6) 39 (2019)
85. Bogdanov A A et al. *St. Petersburg State Polytech. Univ. J. Phys. Math.* **16** 410 (2023) https://doi.org/10.18721/JPM.161.262
86. Verbitskaya E et al. *IEEE Trans. Nucl. Sci.* **49** 258 (2002)
87. Eremin V et al. *Nucl. Instrum. Meth. Phys. Res. A* **583** 91 (2007)
88. Noschis E, Eremin V, Ruggiero G *Nucl. Instrum. Meth. Phys. Res. A* **574** 420 (2007)
89. Eremin V, Verbitskaya E *Nucl. Instrum. Meth. Phys. Res. A* **612** 516 (2010)
90. Li Z et al. *Nucl. Instrum. Meth. Phys. Res. A* **617** 552 (2010)
91. Verbitskaya E et al. *JINST* **11** P12012 (2016)
92. Peltola T et al. *JINST* **12** P09032 (2017)
93. Verbitskaya E M et al. *Semiconductors* **45** 536 (2011); *Fiz. Tekh. Poluprovodn.* **45** 547 (2011)
94. Fadeeva N N "Radiatsionnaya degradatsiya funktsionirovaniya kol'tsevykh struktur v kremnievykh detektorakh yadernykh izluchenii" ("Radiation degradation of the functioning of ring structures in silicon detectors of nuclear radiation"), Thesis for Candidate of the Sci. in Phys. and Math. (SPb.: Saint Petersburg Electrotechnical Univ. "LETI," 2013)
95. Eremin I V "Kriticheskie elementy p–i–n struktur na osnove vysokoomnogo kremniya. Analiz raboty i model'nye predstavleniya" ("Critical elements of p–i–n structures based on high-resistivity silicon. Analysis of work and model representations"), Thesis for Candidate of the Sci. in Phys. and Math. (St. Petersburg: Herzen Univ., 2013)
96. Ruggiero G et al. *Nucl. Instrum. Meth. Phys. Res. A* **604** 242 (2009)
97. Verbitskaya E, Eremin V, Ruggiero G *Nucl. Instrum. Meth. Phys. Res. A* **612** 501 (2010)
98. Verbitskaya E, Eremin V, Ruggiero G *Nucl. Instrum. Meth. Phys. Res. A* **658** 108 (2011)
99. Fretwurst E et al. *Nucl. Instrum. Meth. Phys. Res. A* **514** 1 (2003)
100. Li Z et al. *IEEE Trans. Nucl. Sci.* **51** 1901 (2004)
101. Eremin V K et al. *Semiconductors* **46** 948 (2012); *Fiz. Tekh. Poluprovodn.* **46** 971 (2012)
102. Eremin V et al. *Nucl. Instrum. Meth. Phys. Res. A* **730** 95 (2013)
103. Verbitskaya E et al. *Nucl. Instrum. Meth. Phys. Res. A* **754** 63 (2014)
104. Eremin V, Fadeeva N, Verbitskaya E *JINST* **12** P09005 (2017)
105. Ruggiero G et al. *Nucl. Instrum. Meth. Phys. Res. A* **476** 583 (2002)
106. Kurfürst C et al. *Nucl. Instrum. Meth. Phys. Res. A* **782** 149 (2015)
107. Verbitskaya E et al. *Nucl. Instrum. Meth. Phys. Res. A* **796** 118 (2015)
108. Verbitskaya E et al. *JINST* **12** C03036 (2017)
109. Eremin V et al. *J. Appl. Phys.* **123** 204501 (2018)
110. Eremin V, Shepelev A, Verbitskaya E *JINST* **17** P11037 (2022)
111. Shepelev A S "Transport neravnovesnykh nositelei zaryada v obluchennykh kremnievykh detektorakh pri temperature sverkhtekuchego geliya" ("Transport of nonequilibrium charge carriers in irradiated silicon detectors at the temperature of superfluid helium"), Thesis for Candidate of the Sci. in Phys. and Math. (St. Petersburg: Ioffe Institute, 2003)
112. Eremin V et al. *Nucl. Instrum. Meth. Phys. Res. A* **500** 121 (2003)
113. Verbitskaya E et al. *IEEE Trans. Nucl. Sci.* **52** 1877 (2005)
114. von Schmid M et al. *Nucl. Instrum. Meth. Phys. Res. A* **629** 197 (2011)
115. Sirunyan A M et al. (CMS, TOTEM Collab.) *J. High Energy Phys.* **2018** 153 (2018)
116. Bartosik M R et al., in *Proc. of the IBIC14, September 14–18, 2014, Monterey, CA, USA*, TUPD25
117. Eremin V K et al. *Semiconductors* **43** 796 (2009); *Fiz. Tekh. Poluprovodn.* **43** 825 (2009)
118. Verbitskaya E M et al. *Semiconductors* **45** 536 (2011); *Fiz. Tekh. Poluprovodn.* **45** 547 (2011)